PHOTONICS Research

Learning to recognize misaligned hyperfine orbital angular momentum modes

Xiao Wang,[1] Yufeng Qian,[1] JingJing Zhang,[1] Guangdong Ma,[1] Shupeng Zhao,[1] RuiFeng Liu,[1,*] Hongrong Li,[1] Pei Zhang,[1] Hong Gao,[1] Feng Huang,[2,3] and Fuli Li[1]

[1]Shaanxi Province Key Laboratory of Quantum Information and Quantum Optoelectronic Devices, School of Physics, Xi'an Jiaotong University, Xi'an 710049, China
[2]School of Mechanical Engineering and Automation, Fuzhou University, Fuzhou 350108, China
[3]e-mail: huangf@fzu.edu.cn
*Corresponding author: ruifeng.liu@mail.xjtu.edu.cn

Received 20 October 2020; revised 4 January 2021; accepted 26 January 2021; posted 29 January 2021 (Doc. ID 412965); published 15 March 2021

Orbital angular momentum (OAM)-carrying beams have received extensive attention due to their high-dimensional characteristics in the context of free-space optical communication. However, accurate OAM mode recognition still suffers from reference misalignment of lateral displacement, beam waist size, and initial phase. Here we propose a deep-learning method to exquisitely recognize OAM modes under misalignment by using an alignment-free fractal multipoint interferometer. Our experiments achieve 98.35% recognizing accuracy when strong misalignment is added to hyperfine OAM modes whose Bures distance is 0.01. The maximum lateral displacement we added with respect to the perfectly on-axis beam is about ±0.5 beam waist size. This work offers a superstable proposal for OAM mode recognition in the application of free-space optical communication and allows an increase of the communication capacity.

https://doi.org/10.1364/PRJ.412965

1. INTRODUCTION

It is well known that the orbital angular momentum (OAM) of photons was discovered by Allen *et al.* [1] in 1992. Since the topological charge ℓ can be any integer, the OAM-carrying beams have countless orthogonal eigenstates, which allows them to have high-dimensional characteristics [2]. Benefiting from such high-dimensional characteristics, current applications of free-space optical (FSO) communication with OAM states are widely studied in the lab and real urban environments [3–10]. Naturally, the recognition of OAM modes in the receiving unit is one of the most important tasks for an optical communication system. A Gaussian mode converted by a forked hologram from the target OAM mode is the only mode that couples efficiently into the single-mode fiber [11]. More complicated computational holograms can be designed for the recognition of OAM superposition states [12]. Leach *et al.* presented the cascading additional Mach–Zehnder interferometers with dove prisms, which can sort OAM eigenstates into different paths [13]. By employing the Cartesian to log-polar transformation, one can convert the helically phased light beam corresponding to OAM state into a beam with a transverse phase gradient, and separate OAM eigenstates into different lateral positions [14–17]. Extensive research has also been carried out to characterize OAM modes by letting beams form diffraction patterns by passing through well-designed masks, such as multipoint interference [18], triangular aperture diffraction [19], angular-double-slit interference [20], and gradually changing-period grating [21].

However, all the above OAM mode-recognizing methods require a complicated optical alignment process for FSO communication. Generally, the OAM of a light beam depends on the choice of the reference axis [22]. A pure OAM eigenstate will transform into the superposition of OAM states in a displaced coordinate frame [23] and result in the mixing of information between adjacent modes. In the standard approaches to FSO communication with the polarization of photons, the transmitting and receiving units with a shared reference frame are required. In 2012, Ambrosio *et al.* implemented the quantum communication [24] with hybrid polarization-OAM-entangled states, and this proposal is rotation-immune to the shared reference frame. Displacement of the reference frame also imposes serious obstacles to the application of FSO communication with OAM states. To overcome these obstacles, misalignment correction is implemented by using the mean square value of the OAM spectrum as an indicator [25]. However, OAM spectrum measurement with high precision under the case of misalignment is necessary before the OAM spectrum correction.

Recently, with the rapid increase in computing power, deep learning (DL) [26] has once again become a hot topic in various disciplines. Trained deep neural networks (DNNs) show state-of-the-art performance in imaging through scattering media [27–29], phase retrieval [30,31], structure light recognition [9,32–36], and creating new quantum experiments [37]. A milestone in the history of convolutional neural networks (CNNs) is the appearance of ResNet proposed by He *et al.* [38]. The core of the ResNet model is to establish shortcuts or skip connections between early layers and later layers, which helps in the backpropagation of the gradient during the training process, so as to train a deeper CNN. As a representative of CNNs, DenseNet [39] performs well in the ImageNet data set, it establishes dense connections between all early layers and later layers, and, specifically, each layer accepts all preceding layers as its additional inputs. Another major characteristic of DenseNet is the feature reuse through the connection of features on the channel. These characteristics allow DenseNet to achieve better performance than ResNet with fewer parameters and computational costs.

In this work, we implement an alignment-free fractal multipoint interferometer for hyperfine OAM mode recognition assisted by DL. By using a well-designed fractal multipoint mask (FMM) to sample the complex phase fronts of OAM modes, wealthy diffraction intensity patterns can be recorded for different OAM modes. Meanwhile, the diffraction patterns are stable against reference misalignment because of the inherent periodic structure of the FMM. Stochastic disturbances of three different parameters of the OAM states are set in the experiments: (i) beam waist size $\omega \in [0.45, 0.55]$ mm; (ii) initial phase of OAM states $\varphi_0 \in [0, 2\pi]$; (iii) lateral translation range along the x and y directions $\Delta x, \Delta y \in [-0.25, 0.25]$ mm. Here, the maximum lateral displacement of the FMM we added with respect to the perfectly on-axis beam is about ± 0.5 beam waist size along the x and y directions, respectively. With the above three parameters changing randomly at the same time, we implement the recognition of OAM eigenstates with an accuracy of 100%. Adjacent OAM superposition states with a Bures distance (BD) close to 0.01 are also recognized with an accuracy higher than 98.3%. Benefiting from the simple FMM configuration and superhigh resolution recognition with high accuracy, our detection method is very useful for systems where the optical vortices are expected to be on very large scales, such as in FSO communication [9] and astronomical optical vortices [40].

2. METHODS

The experimental setup is shown in Fig. 1(a). A He–Ne laser with 633 nm wavelength is utilized as light source. After being collimated and expanded, the laser beam is projected on a phase-only spatial light modulator (SLM) (Hamamatsu model X10468) to generate the desired Laguerre–Gaussian (LG) modes. Then the LG modes are imaged on the plane of a digital micromirror device (DMD) (DLP4500, 1140 × 912 diamond pixel array of 7.6 μm × 7.6 μm mirrors) by a 4f imaging system L3 and L4. A well-designed FMM as shown in the inset of Fig. 1(b) is loaded on the DMD. After leaving the DMD plane, the beam passes through lens L5, and the far-field diffraction intensity pattern is collected by a charge-coupled device (CCD) (Lumenera INFINITY3-1C) with 1392 × 1040 pixels. We set the CCD to operate in 12-bit mode. Figure 1(c) shows an example of the recorded diffraction intensity patterns.

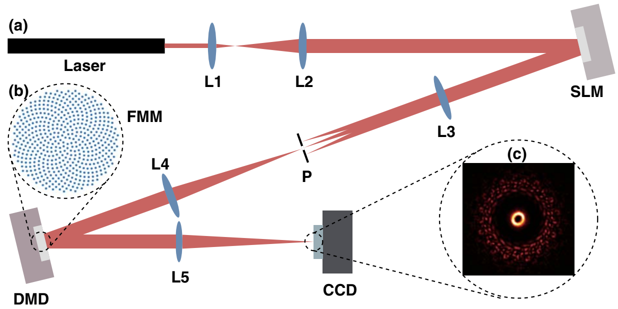

Fig. 1. (a) Alignment-free fractal multipoint interferometer. Laser, He–Ne laser with 633 nm wavelength; L1, 50 mm lens; L2, 500 mm lens; SLM, phase-only spatial light modulator; L3, 300 mm lens; P, pinhole; L4, 300 mm lens; DMD, digital micromirror device; L5, 250 mm lens; CCD, charge-coupled device. (b) proposed FMM; (c) example of the far-field intensity patterns.

The LG modes have a complex field amplitude given by

$$\mathrm{LG}_p^\ell(r,\varphi) \propto r^\ell L_p^\ell\left(\frac{2r^2}{\omega^2}\right) \exp\left(-\frac{r^2}{\omega^2}\right) \exp(-i\ell\varphi), \quad (1)$$

where (r,φ) are the radial and azimuthal coordinates, respectively. ω is the beam waist, and $L_p^\ell(2r^2/\omega^2)$ is the associated Laguerre polynomial. ℓ is the topological charge, and p is the radial mode index. The complex amplitude field after the FMM is

$$U(x,y) = \sum_{n=1}^{N} \mathrm{circ}\left[\frac{\sqrt{(x-x_n)^2+(y-y_n)^2}}{r_0}\right] \mathrm{LG}_p^\ell(r,\varphi), \quad (2)$$

where $\mathrm{circ}(x,y)$ is the transmittance function of the aperture in the FMM, and r_0 is the radius of the FMM aperture. x_n, y_n are the central coordinates of the nth aperture. In the experiments, we implement the lateral translation misalignment by adding random lateral displacement Δx and Δy along the x and y directions, respectively, for the FMM. Here we employ a model for the pattern of florets in the head of a sunflower proposed by Helmut Vogel [41] in 1979 to arrange the position of each aperture, which is given by

$$x_n = C_1\sqrt{n}\cos\left(\frac{2\pi}{C_2^2 n}\right), \qquad y_n = C_1\sqrt{n}\sin\left(\frac{2\pi}{C_2^2 n}\right), \quad (3)$$

where C_1 is the constant scaling factor, and C_2 is the divergence angle. Considering the Fraunhofer limit, the far-field intensity pattern in the detector plane I is given by the Fourier transform of the field in the FMM plane,

$$I \propto |\mathcal{F}[U(x,y)]|^2, \quad (4)$$

and $\mathcal{F}[\cdot]$ represents the Fourier transform.

To estimate the topological charge of the LG modes with the recorded intensity patterns I, we define $I = H(\ell)$, where the $H(\cdot)$ represents the forward physical process that produces the diffraction pattern from the incident LG mode with the topological charge ℓ. The optimization problem can be implicitly written as

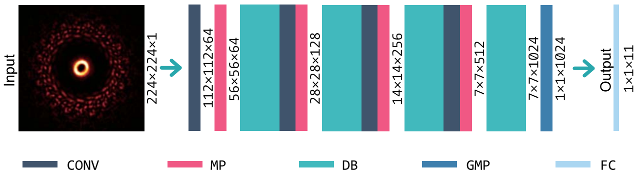

Fig. 2. Schematic diagram of DenseNet-121. CONV, convolution layer; MP, max pooling layer; DB, dense block; GMP, global max pooling layer; FC, fully connected layer.

$$\hat{\ell} = \operatorname{argmin}_{\ell} \mathcal{L}\{H(\ell), I, R(\ell)\}, \tag{5}$$

where $\hat{\ell}$ is the estimate of the inverse, $\mathscr{L}$ is the objective function to minimize, and $R(\ell)$ is the regularizer, or prior knowledge term that imposes constraints on the solution.

Here we adopt an end-to-end DL method, the DenseNet-121, to solve the above optimization problem. The architecture of the DenseNet-121 is shown in Fig. 2. The diffraction intensity patterns collected by the CCD are cropped and resized to 224×224 pixels from raw 1392×1040 pixels, with their corresponding state labels artificially added. The diffraction patterns and labels are paired to form the training set as inputs to the DenseNet-121. Then the inputs are fed to a convolution layer with filter size 7×7 and strides (2, 2) followed by a 3×3 max pooling layer with stride (2, 2). After that, four dense blocks with 6, 12, 24, and 16 convolution units, respectively, are implemented, and a 1×1 convolution layer followed by 2×2 max pooling is utilized as transition layers between two contiguous dense blocks. At the end of the last dense block, a global max pooling is performed; then a fully connected layer with a softmax classifier is attached. In DenseNet-121, rectified linear units (Relus) are used as the activation function, categorical-cross-entropy loss as loss function, and stochastic gradient descent (SGD) as optimizer. It is worth pointing out that the difference between the adjacent superposition states we selected is very small, and the inherent average pooling layer of DenseNet-121 will further weaken this difference. Therefore, we choose a max pooling layer to amplify small differences of the diffraction intensity patterns between different states. The program in our experiment was implemented on the Keras framework with Python 3.5, and sped up by a pair of GPUs (NVIDIA GTX 1080ti).

3. RESULTS

We first perform the DenseNet-121 to recognize LG eigenstates with topological charge $\ell \in \{-5, -4, \cdots, 5\}$ and $p = 0$. In order to test the robustness of the proposed method, stochastic disturbance of three parameters of the OAM states is set simultaneously for the acquisition of each diffraction intensity pattern: (i) beam waist size $\omega \in [0.45, 0.55]$ mm; (ii) initial phase of OAM states $\varphi_0 \in [0, 2\pi]$; (iii) lateral translation range along the x and y directions $\Delta x, \Delta y \in [-0.25, 0.25]$ mm. A total of 1100 experimental diffraction intensity patterns and their corresponding topological charge ℓ as labels are used as the data set, with 100 samples for each topological charge ℓ. All 1100 samples are randomly shuffled, of which the first 850 samples are used as the training set; the remaining 250 samples never participate in the training process.

Figure 3 shows the examples of recorded diffraction intensity patterns for LG eigenstates with topological charge $\ell \in \{0, 1, \pm 2, 5\}$. Figures 3(a1)–3(e1) are diffraction patterns when LG beams are perfectly on-axis. Figures 3(a2)–3(e2) and 3(a3)–3(e3) are diffraction patterns when lateral translations of $\Delta x = \Delta y = 0.15$ mm and 0.25 mm are added on the LG beams, respectively. We collect each diffraction pattern in Fig. 3 by keeping the parameters ω and φ_0 to vary randomly according to the range mentioned above. The diffraction patterns show characters of donut-shaped intensity profile in the center with surrounding asteroid-belt-liked speckles. The patterns in the center keep an intensity profile similar to the input LG eigenstates. The additional asteroid-belt-like speckles behave as completely different intensity profiles resulting from the interference of different spiral wavefronts, and it is helpful for the recognition of LG modes. Since the apertures of the proposed FMM are uniformly distributed from the center to

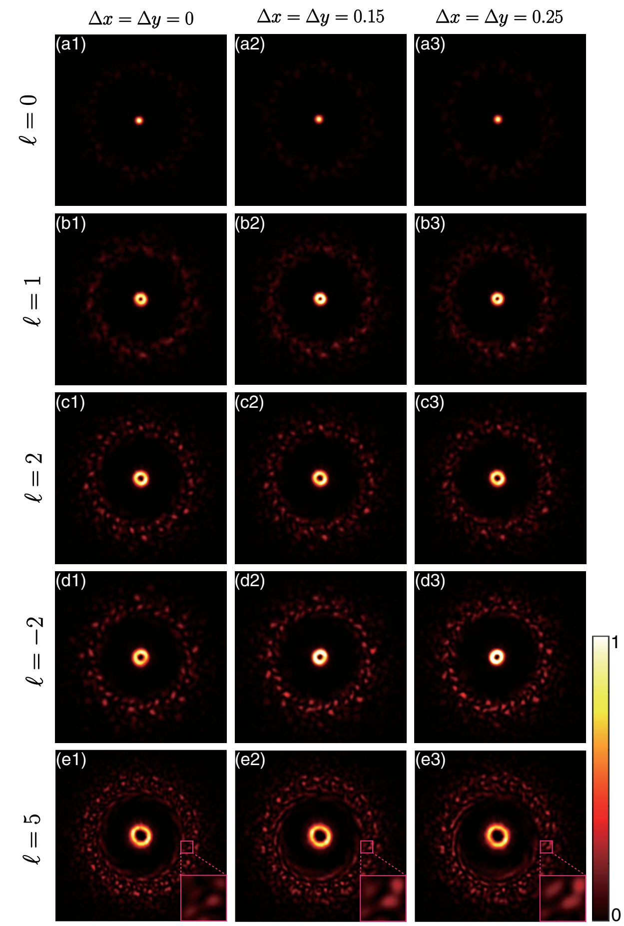

Fig. 3. Examples of the experimental diffraction intensity patterns for LG eigenstates with topological charge $\ell \in \{0, 1, \pm 2, 5\}$ and different FMM displacements $\Delta x = \Delta y \in \{0, 0.15, 0.25\}$ mm. In addition, all the diffraction patterns are obtained with stochastic disturbances of the other two parameters: (i) beam waist size $\omega \in [0.45, 0.55]$ mm; (ii) initial phase of OAM states $\varphi_0 \in [0, 2\pi]$. Insets in (e1)–(e3) show the detailed profiles of the recorded intensity patterns.

the edge according to Eq. (3), it may help to maintain the details of the diffraction patterns to some extent. One can find that the enlarged details of the insets in Figs. 3(e1)–3(e3) are basically retained under different FMM displacements. Furthermore, this distribution of the proposed FMM is asymmetric with respect to any axis in its plane, which contributes to the robustness of distinguishing the diffraction patterns from positive and negative ℓ. After careful tuning, the trained DenseNet-121 is fed with test data to evaluate its ability for classification. A normalized confusion matrix for misaligned LG eigenstates $\ell \in \{-5, -4, \cdots, 5\}$ and $p = 0$ is shown in Fig. 4. All test data are correctly recognized, and an accuracy rate of 100% is achieved. As can be seen from the curves on the top right of Fig. 4, it only took five epochs for the DenseNet-121 to reach 100% accuracy in both the training and test sets. This indicates that the diffraction patterns formed by the LG eigenstates with different topological charge ℓ are quite different and can be easily learned by the DenseNet-121 to achieve accurate classification.

To further demonstrate the performance of the proposed method, we experimentally implement the recognition of hyperfine OAM superposition states. We choose two mutually orthogonal bases, $|\ell = \pm 1\rangle$, to construct the Bloch sphere, and each point on the sphere is a superposition state constructed by this set of bases. As shown in Fig. 5(a), the state $|\psi\rangle$ represented by an arbitrary point on the Bloch sphere is given by

$$|\psi\rangle = \cos\frac{\theta}{2}|1\rangle + \sin\frac{\theta}{2}e^{i\phi}|-1\rangle, \quad (6)$$

where θ is the polar angle and ϕ is the azimuthal angle. We take 200 and 400 points uniformly from $[0, \pi]$ and $[0, 2\pi]$ according to the respective ranges of θ and ϕ. In this way, 80,000 points with an interval of 0.005π evenly distributed on the spherical surface are obtained, as schematically shown in Fig. 5(b). Without loss of generality, we randomly select an area on the Bloch sphere with nine superposition states. The nine superposition states combined by θ and ϕ are shown in Table 1, and we name them Modes 1–9 for convenience. The values of θ are 0.52π, 0.525π, and 0.53π, while the values of ϕ are 0.02π, 0.025π, and 0.03π. The red box in Fig. 5(b) schematically shows the position distribution of the nine superposition states on the Bloch sphere. We utilize the BD [42] $D_B^2[\rho_A, \rho_B] = 2[1 - \sqrt{F(\rho_A, \rho_B)}]$, where $F(\rho_A, \rho_B) = [\mathrm{Tr}\sqrt{\sqrt{\rho_A}\rho_B\sqrt{\rho_A}}]^2$ is the fidelity of the two states, to calculate the distance between adjacent modes ρ_A and ρ_B on the Bloch sphere. The distance between two horizontal (e.g., Modes 4 and 7) or vertical (e.g., Modes 1 and 2) adjacent modes of the nine modes we selected on the Bloch sphere is 0.01, while the distance between diagonally positioned adjacent modes (e.g., Modes 5 and 9) is 0.015. This means that any two adjacent modes are so similar that their corresponding diffraction patterns are also very similar and difficult to recognize.

In the experiments, stochastic disturbances of parameters, (i) beam waist size $\omega \in [0.45, 0.55]$ mm, (ii) initial phase $\varphi_0 \in [0, 2\pi]$, and (iii) lateral translation $\Delta x, \Delta y \in [-0.25, 0.25]$ mm, are also introduced in these superposition states. A total of 9000 recorded diffraction intensity patterns and their corresponding labels are used as the data set: 1000 samples for each category, 7000 of which are used as the training set and 2000 are used as the test set. The diffraction intensity patterns for superposition states of Mode 4, Mode 5, and Mode 6 under different stochastic disturbances of the above three parameters are shown in Figs. 6(a1)–6(c3). Similar to the results of eigenstates, the diffraction patterns for superposition states also consist of two parts: central lobes that have the similar intensity profile to the input superposition states and the surrounding asteroid-belt-like speckles. One can see that the diffraction patterns formed by different superposition states are highly

Table 1. Nine Superposition States Combined by θ and ϕ

	$\phi = 0.020\pi$	$\phi = 0.025\pi$	$\phi = 0.030\pi$
$\theta = 0.520\pi$	Mode 1	Mode 4	Mode 7
$\theta = 0.525\pi$	Mode 2	Mode 5	Mode 8
$\theta = 0.530\pi$	Mode 3	Mode 6	Mode 9

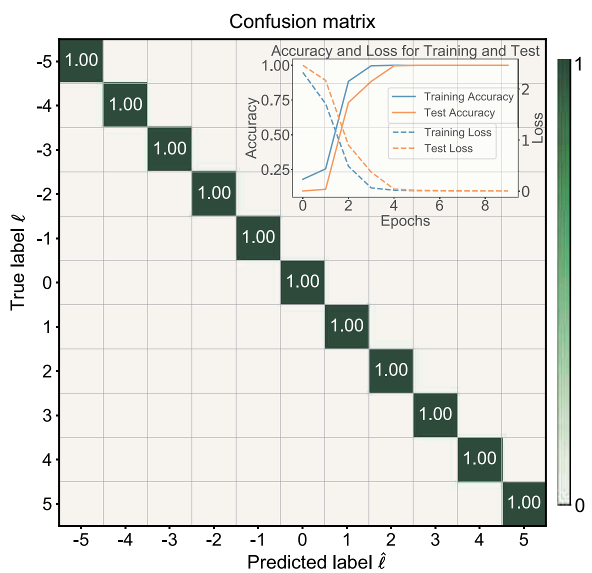

Fig. 4. Confusion matrix for the recognition of misaligned LG eigenstates $\ell \in \{-5, -4, \cdots, 5\}$ and $p = 0$, with the curves of accuracy and loss as functions of epochs on the top right.

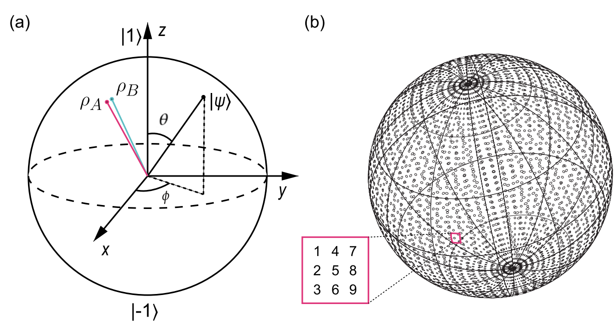

Fig. 5. Schematic diagram of a Bloch sphere constructed with $|\ell = \pm 1\rangle$ bases. (a) An arbitrary state $|\psi\rangle$ on the sphere and two adjacent superposition states ρ_A and ρ_B; (b) sphere is divided into 80,000 points corresponding to 80,000 states; the red box schematically indicates the position distribution of the nine selected superposition states for the experiments.

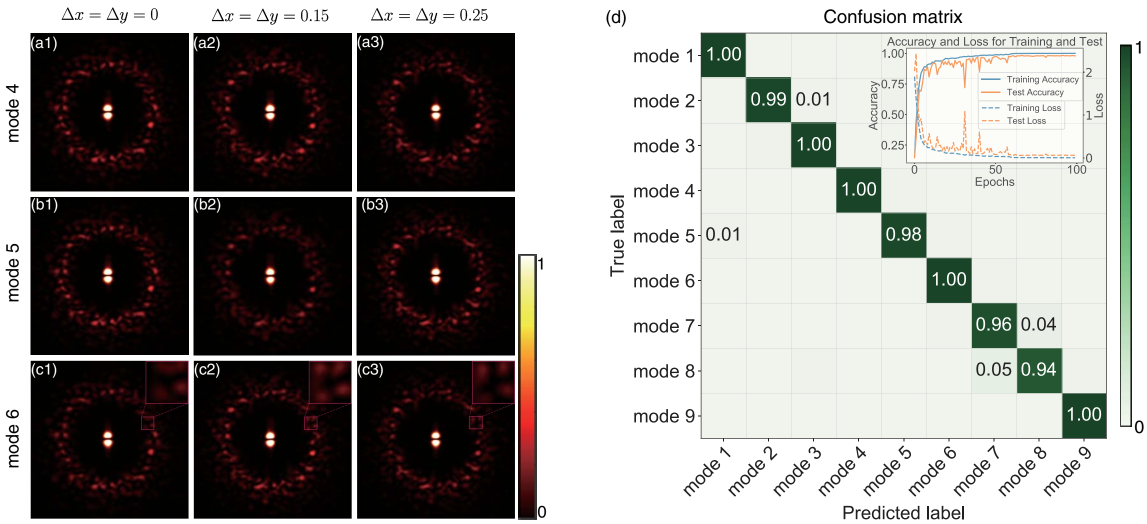

Fig. 6. Experimental results of hyperfine LG superposition states. (a)–(c) Examples of the recorded diffraction intensity patterns for OAM superposition states under different misaligned configurations. The collection of each diffraction pattern in the figure is carried out with stochastic disturbances of the other two parameters: (i) beam waist size $\omega \in [0.45, 0.55]$ mm; (ii) initial phase of OAM states $\varphi_0 \in [0, 2\pi]$. To show the image clearly, we reduce the contrast of the image by setting the values of $I = 0.3 \times \max\{I\}$, where $I > 0.3 \times \max\{I\}$; (d) confusion matrix for superposition states from Mode 1 to Mode 9 with the curves of accuracy and loss as functions of epochs on the top right.

semblable. However, the well-tuned DenseNet-121 achieved an accuracy of 98.35%, and only a small number of adjacent states are misjudged, as shown in Fig. 6(d). The recognition accuracy of superposition states is lower than that of eigenstates, but it is still improving. Compared with eigenstates, the training of superposition states is obviously more time-consuming, as shown in the curves on the top right of Fig. 6(d). This is because the superposition states require more training samples and the similarity between the superposition states is large, which makes it difficult for them to converge. On the one hand, the disturbance of the experimental device or the environment is likely to have a huge impact on the experimental results when the adjacent superposition states are highly similar. On the other hand, the roughly retained details in the insets of Figs. 6(c1)–6(c3) and the raise in the number of training data help DenseNet-121 achieve better feature extraction. In fact, if one reduces the intensity of the illumination laser beam, the asteroid-belt-like speckles will be drowning in the electron noise of the camera. The predictive accuracy of the hyperfine OAM states is reduced as we lose the detailed information of the asteroid-belt-liked speckles.

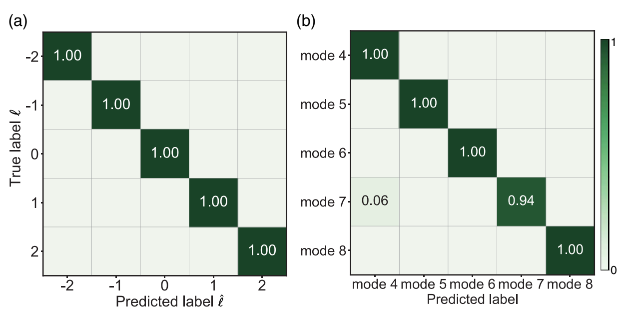

Fig. 7. Confusion matrix of LG modes with $p = 1$. (a) Confusion matrix for LG eigenstates of $\ell \in \{-2, -1, \cdots, 2\}$ and $p = 1$; (b) confusion matrix for superposition states from Mode 4 to Mode 8. Mode 4 to Mode 8 here represent the superposition states with $p = 1$ at the same positions on the Bloch sphere in the case of $p = 0$.

Here, to fully demonstrate the robustness of the proposed method, we implement the hyperfine OAM mode recognition for the case of $p \neq 0$. In experiments, we set $p = 1$, and all other conditions remain the same as the above experiments. The normalized partial confusion matrices of the eigenstates $\ell \in \{-2, -1, \cdots, 2\}$ and superposition states of Mode 4 to Mode 8 in Table 1 are shown in Figs. 7(a) and 7(b), respectively. Similar to the result in the case of $p = 0$, the DenseNet-121 easily realized an accuracy of 100% for the eigenstates, and an accuracy of 98.82% for superposition states with the radial mode index $p = 1$.

4. CONCLUSION

In conclusion, we experimentally implemented hyperfine OAM mode recognition under strong misalignment by using an alignment-free fractal multipoint interferometer assisted by DL. The misalignment includes three stochastic disturbances of parameters: (i) beam waist size $\omega \in [0.45, 0.55]$ mm; (ii) initial phase $\varphi_0 \in [0, 2\pi]$; (iii) lateral translation $\Delta x, \Delta y \in [-0.25, 0.25]$ mm. Here, the maximum lateral misalignment of the FMM we added with respect to the perfectly on-axis beam is about ± 0.5 beam waist size along the x and y directions, respectively. The well-tuned DenseNet-121 is demonstrated to be robust for recognizing very similar superposition states with a small BD of 0.01 between adjacent modes under the above strong misalignment. Benefiting from the robustness of the proposed method and simple FMM configuration, this scheme shows potential application for FSO communication where the optical vortices are expected to be on a large scale and the misalignment between the transmitting and receiving units is inevitable.

Funding. National Natural Science Foundation of China (11534008, 91736104); Ministry of Science and Technology of the People's Republic of China (2016YFA0301404); Fundamental Research Funds for the Central Universities.

Disclosures. The authors declare no conflicts of interest.

REFERENCES

1. L. Allen, M. W. Beijersbergen, R. Spreeuw, and J. Woerdman, "Orbital angular momentum of light and the transformation of Laguerre-Gaussian laser modes," Phys. Rev. A **45**, 8185–8189 (1992).
2. A. M. Yao and M. J. Padgett, "Orbital angular momentum: origins, behavior and applications," Adv. Opt. Photon. **3**, 161–204 (2011).
3. A. Vaziri, G. Weihs, and A. Zeilinger, "Experimental two-photon, three-dimensional entanglement for quantum communication," Phys. Rev. Lett. **89**, 240401 (2002).
4. G. Gibson, J. Courtial, M. J. Padgett, M. Vasnetsov, V. Pas'ko, S. M. Barnett, and S. Franke-Arnold, "Free-space information transfer using light beams carrying orbital angular momentum," Opt. Express **12**, 5448–5456 (2004).
5. J. Wang, J.-Y. Yang, I. M. Fazal, N. Ahmed, Y. Yan, H. Huang, Y. Ren, Y. Yue, S. Dolinar, M. Tur, and A. E. Willner, "Terabit free-space data transmission employing orbital angular momentum multiplexing," Nat. Photonics **6**, 488–496 (2012).
6. N. Bozinovic, Y. Yue, Y. Ren, M. Tur, P. Kristensen, H. Huang, A. E. Willner, and S. Ramachandran, "Terabit-scale orbital angular momentum mode division multiplexing in fibers," Science **340**, 1545–1548 (2013).
7. M. Krenn, R. Fickler, M. Fink, J. Handsteiner, M. Malik, T. Scheidl, R. Ursin, and A. Zeilinger, "Communication with spatially modulated light through turbulent air across Vienna," New J. Phys. **16**, 113028 (2014).
8. A. E. Willner, H. Huang, Y. Yan, Y. Ren, N. Ahmed, G. Xie, C. Bao, L. Li, Y. Cao, Z. Zhao, J. Wang, M. P. J. Lavery, M. Tur, S. Ramachandran, A. F. Molisch, N. Ashrafi, and S. Ashrafi, "Optical communications using orbital angular momentum beams," Adv. Opt. Photon. **7**, 66–106 (2015).
9. M. Krenn, J. Handsteiner, M. Fink, R. Fickler, R. Ursin, M. Malik, and A. Zeilinger, "Twisted light transmission over 143 km," Proc. Natl. Acad. Sci. USA **113**, 13648–13653 (2016).
10. M. P. Lavery, C. Peuntinger, K. Günthner, P. Banzer, D. Elser, R. W. Boyd, M. J. Padgett, C. Marquardt, and G. Leuchs, "Free-space propagation of high-dimensional structured optical fields in an urban environment," Sci. Adv. **3**, e1700552 (2017).
11. A. Mair, A. Vaziri, G. Weihs, and A. Zeilinger, "Entanglement of the orbital angular momentum states of photons," Nature **412**, 313–316 (2001).
12. E. Bolduc, N. Bent, E. Santamato, E. Karimi, and R. W. Boyd, "Exact solution to simultaneous intensity and phase encryption with a single phase-only hologram," Opt. Lett. **38**, 3546–3549 (2013).
13. J. Leach, M. J. Padgett, S. M. Barnett, S. Franke-Arnold, and J. Courtial, "Measuring the orbital angular momentum of a single photon," Phys. Rev. Lett. **88**, 257901 (2002).
14. G. C. Berkhout, M. P. Lavery, J. Courtial, M. W. Beijersbergen, and M. J. Padgett, "Efficient sorting of orbital angular momentum states of light," Phys. Rev. Lett. **105**, 153601 (2010).
15. M. Mirhosseini, M. Malik, Z. Shi, and R. W. Boyd, "Efficient separation of the orbital angular momentum eigenstates of light," Nat. Commun. **4**, 2781 (2013).
16. Y. Wen, I. Chremmos, Y. Chen, J. Zhu, Y. Zhang, and S. Yu, "Spiral transformation for high-resolution and efficient sorting of optical vortex modes," Phys. Rev. Lett. **120**, 193904 (2018).
17. Y. Wen, I. Chremmos, Y. Chen, G. Zhu, J. Zhang, J. Zhu, Y. Zhang, J. Liu, and S. Yu, "Compact and high-performance vortex mode sorter for multi-dimensional multiplexed fiber communication systems," Optica **7**, 254–262 (2020).
18. G. C. Berkhout and M. W. Beijersbergen, "Method for probing the orbital angular momentum of optical vortices in electromagnetic waves from astronomical objects," Phys. Rev. Lett. **101**, 100801 (2008).
19. J. Hickmann, E. Fonseca, W. Soares, and S. Chávez-Cerda, "Unveiling a truncated optical lattice associated with a triangular aperture using light's orbital angular momentum," Phys. Rev. Lett. **105**, 053904 (2010).
20. R. Liu, J. Long, F. Wang, Y. Wang, P. Zhang, H. Gao, and F. Li, "Characterizing the phase profile of a vortex beam with angular-double-slit interference," J. Opt. **15**, 125712 (2013).
21. K. Dai, C. Gao, L. Zhong, Q. Na, and Q. Wang, "Measuring OAM states of light beams with gradually-changing-period gratings," Opt. Lett. **40**, 562–565 (2015).
22. G. Molina-Terriza, J. P. Torres, and L. Torner, "Management of the angular momentum of light: preparation of photons in multidimensional vector states of angular momentum," Phys. Rev. Lett. **88**, 013601 (2001).
23. M. Vasnetsov, V. Pas'ko, and M. Soskin, "Analysis of orbital angular momentum of a misaligned optical beam," New J. Phys. **7**, 46 (2005).
24. V. D'Ambrosio, E. Nagali, S. P. Walborn, L. Aolita, S. Slussarenko, L. Marrucci, and F. Sciarrino, "Complete experimental toolbox for alignment-free quantum communication," Nat. Commun. **3**, 961 (2012).
25. Y.-D. Liu, C. Gao, X. Qi, and H. Weber, "Orbital angular momentum (OAM) spectrum correction in free space optical communication," Opt. Express **16**, 7091–7101 (2008).
26. Y. LeCun, Y. Bengio, and G. Hinton, "Deep learning," Nature **521**, 436–444 (2015).
27. M. Lyu, H. Wang, G. Li, S. Zheng, and G. Situ, "Learning-based lensless imaging through optically thick scattering media," Adv. Photon. **1**, 036002 (2019).
28. Y. Li, Y. Xue, and L. Tian, "Deep speckle correlation: a deep learning approach toward scalable imaging through scattering media," Optica **5**, 1181–1190 (2018).
29. Y. Sun, J. Shi, L. Sun, J. Fan, and G. Zeng, "Image reconstruction through dynamic scattering media based on deep learning," Opt. Express **27**, 16032–16046 (2019).
30. M. Deng, S. Li, A. Goy, I. Kang, and G. Barbastathis, "Learning to synthesize: robust phase retrieval at low photon counts," Light Sci. Appl. **9**, 1 (2020).
31. A. Goy, K. Arthur, S. Li, and G. Barbastathis, "Low photon count phase retrieval using deep learning," Phys. Rev. Lett. **121**, 243902 (2018).
32. Q. Zhao, S. Hao, Y. Wang, L. Wang, X. Wan, and C. Xu, "Mode detection of misaligned orbital angular momentum beams based on convolutional neural network," Appl. Opt. **57**, 10152–10158 (2018).
33. Z. Liu, S. Yan, H. Liu, and X. Chen, "Superhigh-resolution recognition of optical vortex modes assisted by a deep-learning method," Phys. Rev. Lett. **123**, 183902 (2019).
34. P. Wang, J. Liu, L. Sheng, Y. He, W. Xiong, Z. Huang, X. Zhou, Y. Li, S. Chen, X. Zhang, and D. Fan, "Convolutional neural network-assisted optical orbital angular momentum recognition and communication," IEEE Access **7**, 162025 (2019).
35. S. Sharifi, Y. Banadaki, G. Veronis, and J. P. Dowling, "Towards classification of experimental Laguerre–Gaussian modes using convolutional neural networks," Opt. Eng. **59**, 076113 (2020).
36. T. Giordani, A. Suprano, E. Polino, F. Acanfora, L. Innocenti, A. Ferraro, M. Paternostro, N. Spagnolo, and F. Sciarrino, "Machine learning-based classification of vector vortex beams," Phys. Rev. Lett. **124**, 160401 (2020).
37. A. A. Melnikov, H. P. Nautrup, M. Krenn, V. Dunjko, M. Tiersch, A. Zeilinger, and H. J. Briegel, "Active learning machine learns to create new quantum experiments," Proc. Natl. Acad. Sci. USA **115**, 1221–1226 (2018).
38. K. He, X. Zhang, S. Ren, and J. Sun, "Deep residual learning for image recognition," in *Proceedings of the IEEE Conference on Computer Vision and Pattern Recognition* (2016), pp. 770–778.
39. G. Huang, Z. Liu, L. Van Der Maaten, and K. Q. Weinberger, "Densely connected convolutional networks," in *Proceedings of the IEEE Conference on Computer Vision and Pattern Recognition* (2017), pp. 4700–4708.
40. M. Harwit, "Photon orbital angular momentum in astrophysics," Astrophys. J. **597**, 1266–1270 (2003).
41. H. Vogel, "A better way to construct the sunflower head," Math. Biosci. **44**, 179–189 (1979).
42. J. Dajka, J. Łuczka, and P. Hänggi, "Distance between quantum states in the presence of initial qubit-environment correlations: a comparative study," Phys. Rev. A **84**, 032120 (2011).